Metals and Materials International (2024) 30:2523–2539
https://doi.org/10.1007/s12540-024-01656-2

Effect of YSZ Particle Size and Content on Microstructure, Mechanical and Tribological Properties of $(CoCrFeNiAl)_{1-x}(YSZ)_x$ High Entropy Alloy Composites

M. Ghanbariha[1] · M. Farvizi[1] · S. A. Ataie[2] · A. Alizadeh Samiyan[1] · T. Liskiewicz[3] · H. S. Kim[4,5]

Received: 29 December 2023 / Accepted: 19 February 2024 / Published online: 29 March 2024

Abstract

High entropy alloy composites (HEACs) have recently been explored for use in industrial applications. This study investigates the impact of particle size (micro or nano) and content (5 and 10 wt%) of YSZ on the microstructure and tribological properties of AlCoCrFeNi. The samples were prepared using a combination of mechanical alloying and spark plasma sintering. XRD results and Rietveld analysis reveal that HEACs with micro-sized YSZ have a higher BCC/FCC ratio. FESEM and EDS results confirmed the evolution of Al-rich regions in the vicinity of the reinforcements. Especially, in HEA-10NanoYSZ-sample, due to higher interfacial regions, a huge amount of Al-rich phase has been formed which yields the reduction of BCC phase content in this sample. Microhardness and pin-on-disc wear tests show that the samples reinforced with microparticles demonstrate better performance compared to nanocomposite samples. For example, HEA-10MicroYSZ-sample exhibits the highest hardness (5.1 GPa) and the lowest wear characteristics (with a coefficient of friction of 0.8 and a wear rate of 4×10^{-4} mm^3/N.m). This can be correlated to the higher hardness and BCC phase content, and grain boundary strengthening in the microcomposites.

Keywords High entropy alloy composites · Micro/nano YSZ particles · Microstructure · Hardness · Wear

1 Introduction

Before the year 2004, industrial metallic parts were typically produced using binary or ternary alloys. However, a new class of materials called high entropy alloys (HEAs) emerged after this period [1–3]. HEAs are created by combining multiple elements using various production methods. HEAs can be produced by melting and casting, additive manufacturing, mechanical alloying, spark plasma sintering (SPS), and deposition techniques [4–9]. HEAs have gained considerable attention in a wide range of industries and advanced multi-functional applications. They find applications in diverse fields such as medical parts [10], molds and marine structures [11], electrodes for water electrolysis [12], mechanical components, aerospace, and high-temperature parts [13]. HEAs are characterized by the presence of at least five metallic elements and can be broadly classified into two categories: equimolar and non-equimolar types. Each constituent element should have an atomic percentage of at least 5% to meet the condition for entropy, which is required to be at least 1.5R (where R represents the gas constant). These multi-element alloys exhibit significant

✉ M. Farvizi
mmfarvizi@yahoo.com; mmfarvizi@merc.ac.ir

S. A. Ataie
ata.sayedalireza@gmail.com

1 Department of Ceramic, Materials and Energy Research Center, Karaj 31787-316, Iran

2 School of Metallurgy and Materials Engineering, Iran University of Science and Technology, Narmak, Tehran 16846–13114, Iran

3 Department of Engineering, Faculty of Science and Engineering, Manchester Metropolitan University, Manchester M1 5GD, UK

4 Graduate Institute of Ferrous and Energy Material Technology, Pohang University of Science and Technology, Pohang 37673, Republic of Korea

5 Advanced Institute for Materials Research (WPI-AIMR), Tohoku University, Sendai 980-8577, Japan

improvements in their physical and mechanical properties. These advancements can be attributed to the unique microstructure of HEAs, which is a result of the high content of different metals present. The presence of multiple elements contributes to sluggish diffusion, severe lattice distortion, and the cocktail effect. These distinctive features ultimately lead to enhanced hardness, yield strength, ductility, oxidation resistance, and thermal stability [14, 15].

While a wide range of metallic elements can be utilized in the production of HEAs, transition metals are commonly employed. Fe, Cr, Co, and Ni are easily dissolved due to the atom substitution rules, which take into account factors like enthalpy of mixing, electronegativity, and atomic size. Therefore, the typical composition of an HEA system consists of FeCoCrNi + M, where M represents elements such as Al, Ti, Mn, or Cu [9, 16–20]. Al plays a vital role as the major alloying element in most HEAs, primarily due to its stabilizing effect on both FCC and BCC phases. Consequently, the AlCoCrFeNi system has been extensively studied in numerous research papers and the optimum content of each element is nearly investigated to have higher mechanical properties [21–26]. Each property of HEAs is highly affected by the microstructure, which is influenced by several key factors, including grain size, shape and distribution of secondary phases, as well as the presence of dislocations and twinning. It is worth noting that the microstructure in this system typically consists of a solid solution with one or two phases. Therefore, the ratio of FCC to BCC phases is of utmost importance, as it can significantly impact the physical and mechanical properties of the HEA. Generally, BCC HEAs tend to exhibit high strength, while FCC structures often demonstrate enhanced fracture strain and toughness [27, 28]. However, it should be noted that high entropy alloys (which predominantly consist of metallic elements) often exhibit limited load-bearing capacity and possess moderate hardness and wear resistance. Therefore, there is a need to introduce an enhanced system to address these limitations.

The incorporation of a reinforcement phase has been proven to significantly enhance the hardness and tribological properties of HEAs, particularly through the introduction of ceramic particles. This novel system, known as metal matrix composites (MMCs [29]), involves combining HEAs with carbides (such as WC, TiC [30, 31]), nitrides (such as TiN [32]), or oxides (such as ZrO_2, Al_2O_3 and Y_2O_3 [33–35]). The addition of ceramic particles has the potential to augment mechanical properties through two primary mechanisms: reduction of the average grain size and hindrance of dislocation movement, attributable to the strengthening effect at the grain boundaries [31–36]. In the case of high entropy alloy composites (HEACs), which consist of dissimilar materials (metals and ceramics), it is crucial to have two materials with compatible physical properties. This compatibility is essential in order to minimize the undesired effects of mismatch and distortion. Hence, oxides are typically the preferred choice among various ceramic particles. In general, this preference arises from their inherent advantages, including better chemical stability and adhesion to the parent phase (they have coefficient of thermal expansion values near HEAs) [37]. Moreover, oxides usually show lower friction coefficients and wear rates (which can be attributed to their lower shear strength) [38]. Hence, the utilization of oxide-dispersion strengthening (ODS) represents a promising approach for augmenting the strength of metallic alloys, particularly HEAs. The addition of micro-sized Y_2O_3, Al_2O_3, and ZrO_2 particles to HEAs has been shown to enhance hardness, compressive yield strength, and reduce wear. In the recent articles [39, 40], the authors specifically examined the impact of incorporating micro-sized ZrO_2 particles into the AlCoCrFeNi alloy. Several studies [33, 34, 41] have examined the impact of incorporating nano-sized ZrO_2, Al_2O_3, and Y_2O_3 on the mechanical properties of HEAs. However, due to the presence of multiple strengthening mechanisms in ODS-HEACs (such as grain boundary strengthening, the Hall–Petch mechanism, solid solution strengthening, and Orowan strengthening [42, 43]) the size and content of reinforcement particles present a complex challenge. This is because the mechanical responses can be significantly altered by the same oxide particle with different sizes or content.

Among various oxides, Yttria Stabilized Zirconia (YSZ) is the preferred choice due to its unique properties. The primary advantage of utilizing YSZ lies in its stability and robust thermal shock resistance. Because during the heat treatment of zirconia, a transformation occurs from the tetragonal to monoclinic phases. This transformation is accompanied by a 3–4 vol% expansion, which can have a detrimental impact on the performance of composites. To address this issue, the addition of Y_2O_3 dopant can stabilize the tetragonal phase of zirconia, resulting in what is known as Yttria Stabilized Zirconia [44]. In addition, YSZ represents a high thermal expansion coefficient which plays a crucial role in ensuring interface compatibility between oxide particles and the metal matrix [45]. Moreover, first-principles calculations [46] have demonstrated that the addition of yttria to zirconia can lead to increased hardness and decreased elastic modulus. Therefore, based on the theory that fracture toughness is directly proportional to the H/E ratio [47, 48], it can be inferred that the addition of yttria can improve fracture toughness. It was verified that YSZ exhibits high compressive strength and under mechanical loading, YSZ undergoes a stress-induced transformation that serves to augment its fracture toughness [49]. Also, another

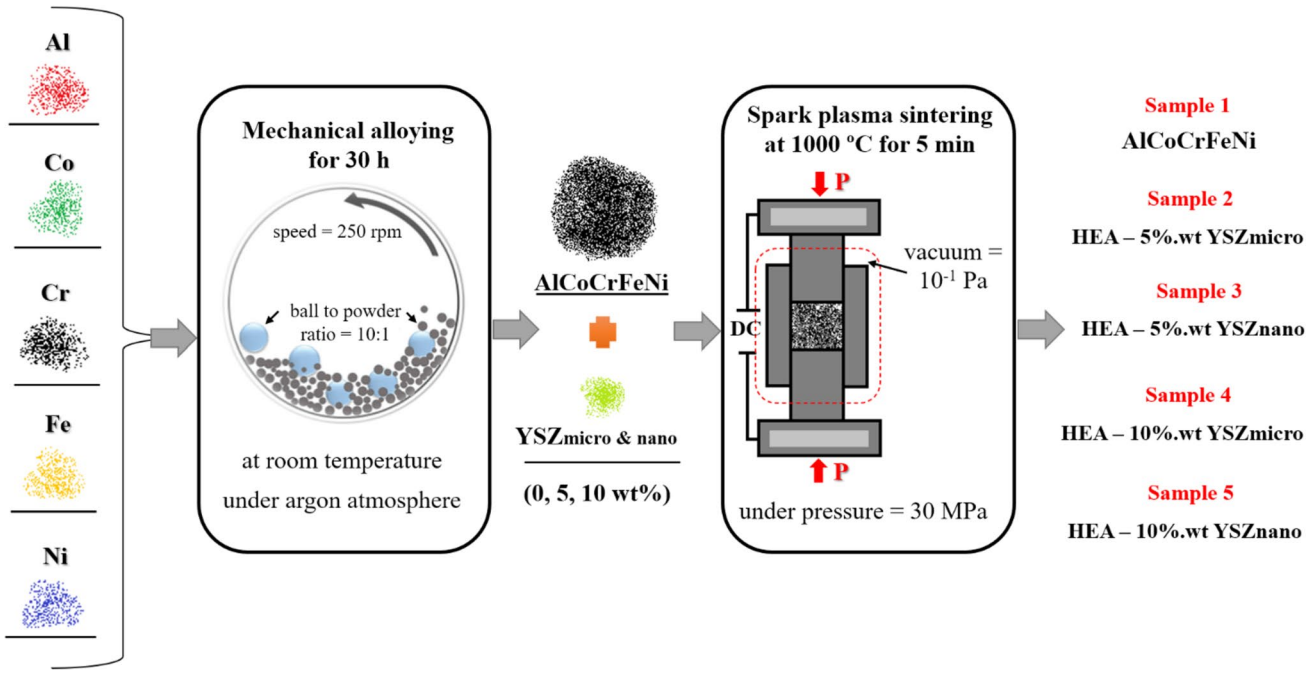

Fig. 1 MA and SPS production schematic

piece of evidence from Raja et al. [50] confirms that YSZ has higher fracture toughness compared to both zirconia and zirconia-toughened alumina. However, investigations into the effects of adding YSZ particles on microstructure and mechanical properties are relatively scarce in the literature. The previous literature primarily focuses on examining the impact of incorporating ZrO_2, Al_2O_3, and Y_2O_3 (rather than YSZ) into HEAs on their mechanical properties. Furthermore, comprehensive surface characteristics (encompassing hardness, wear properties such as friction coefficient and wear rate, and phase structure through Raman analysis simultaneously) of analogous ODS-HEACs have not yet been documented.

The primary aim of this paper is to investigate the influences of YSZ size (nano or micro) and content (5 wt% or 10 wt%) on the morphology and phase structure of AlCoCrFeNi

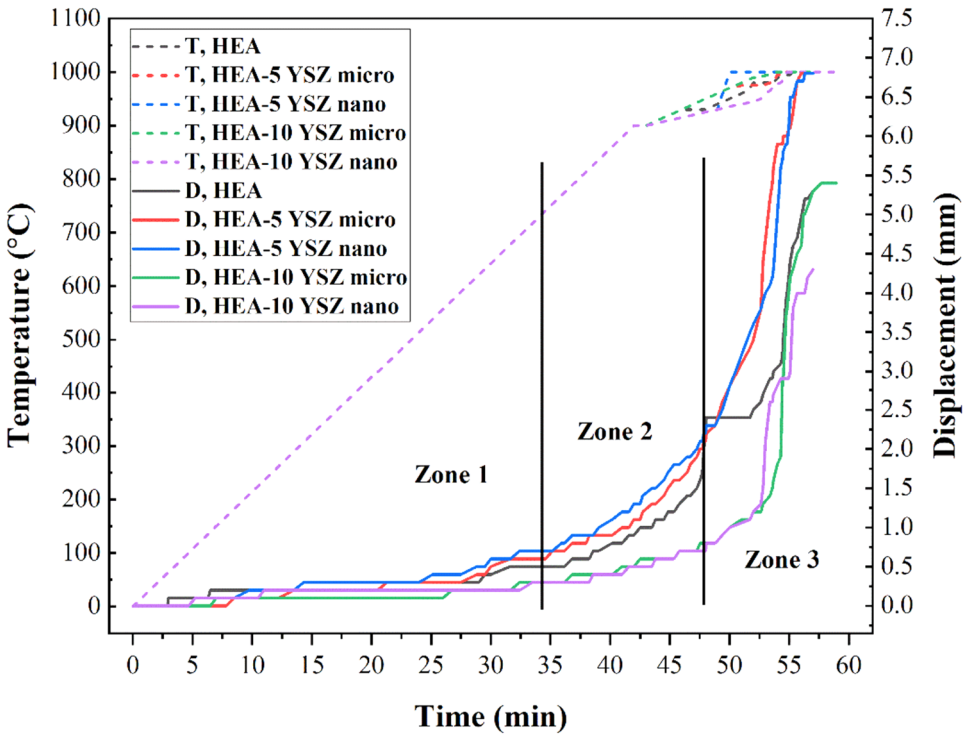

Fig. 2 Variation of SPS temperature and punch displacement against sintering time during the SPS process of HEA-YSZ composites

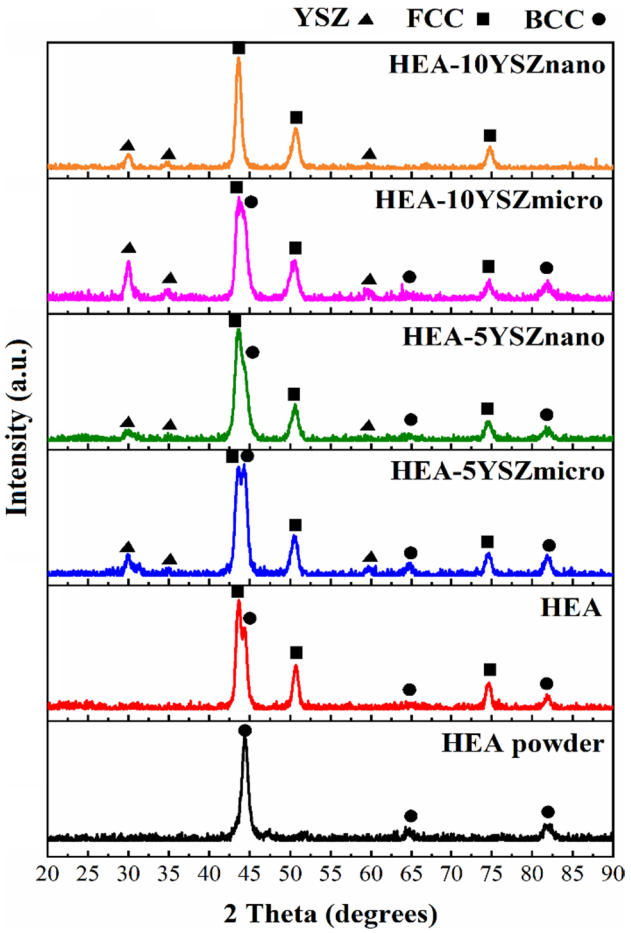

Fig. 3 XRD analysis for **a** HEA powder [39], **b** HEA [39], **c** HEA-5 wt% YSZmicro, **d** HEA-5 wt% YSZnano, **e** HEA-10 wt% YSZmicro, and **f** HEA-10 wt% YSZnano samples

high-entropy alloys (with XRD, SEM/EDS, and Raman spectroscopy techniques). To fabricate these ODS-HEAC samples, a combination of mechanical alloying and spark plasma sintering techniques is employed. Consequently, a comprehensive analysis of the hardness and wear characteristics of the HEA composites will be conducted through indentation and sliding tests. Finally, a discussion will be presented to elucidate the relationships between the microstructure and mechanical properties of the materials. As YSZ levels were selected identically (5 and 10 wt%), the comparison between composites with nano-sized particles and those with micro-sized particles allows for a better understanding of the effects of particle size on the microstructure and performance of the HEAs. This comparison can provide valuable insights into the potential advantages and limitations of using nano-sized particles in composite materials.5

2 Materials and Methods

2.1 Sample Production

Micro-sized metal particles (particle size was lower than 45 µm) with a purity degree exceeding 99% were utilized as the initial materials. These metal particles included aluminum (manufactured by Xinji Guangyuan), Co-Cr-Fe (produced by Merck), and nickel (obtained from Aldrich). Additionally, micro-sized YSZ (ZrO_2-8 wt%Y_2O_3 ~15 µm) and nano-sized YSZ (40–60 nm, Aldrich) were employed as ceramic reinforcements. The powders exhibited a spherical shape. The aforementioned powders underwent mechanical alloying followed by sintering using the SPS technique. A schematic of the combinational procedure is depicted in Fig. 1. Additionally, for a detailed perspective, temperature-displacement curves of the samples using the SPS method are illustrated in Fig. 2. For this particular study, a total of five samples were prepared, each differing in terms of the YSZ size and content. Additional information and supporting data are available in references [40].

2.2 Characterization Methods

X-ray diffraction (XRD) analysis was conducted using a Siemens-Germany D-500 instrument, operating with Cu Kα radiation (λ = 1.54 Å), to perform phase analysis. Furthermore, the phase contents of the samples were determined through Rietveld refinement analysis, employing MAUD software. The morphology and elemental analysis of the samples were evaluated using scanning electron microscopy (SEM) equipped with energy-dispersive spectroscopy (EDS). The SEM–EDS analysis was carried out using a TESCAN MIRA3 instrument from Czech Republic. In addition, Raman spectroscopy (Uni-DRON, South Korea) was employed to investigate the bond structure of each sample, both before and after the sliding test. An Ar-ion laser with midrange Rayleigh wavelength (532 nm) was utilized, and the resolution was set at 1 cm^{-1}. It is important to note that prior to the analysis of Raman spectra, it is advisable to remove any noise and apply baseline correction.

To mitigate the roughness effect, the surface of the samples was polished using a diamond probe with a contact load of 0.1 mN prior to conducting mechanical tests. Subsequently, the surfaces were cleaned using cotton swabs. Microhardness measurements were performed utilizing the Vickers microhardness indenter (FM-600, Future-Tech Corp, Japan). To ensure accuracy and reliability, multiple measurements were taken for each sample from distinct regions, with a minimum of five repetitions.

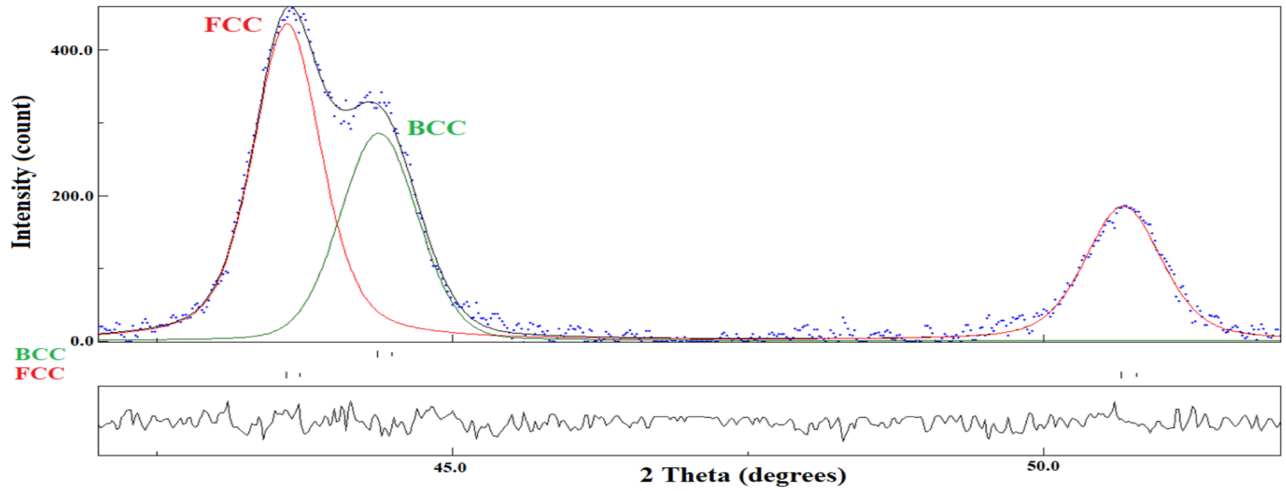

(a)

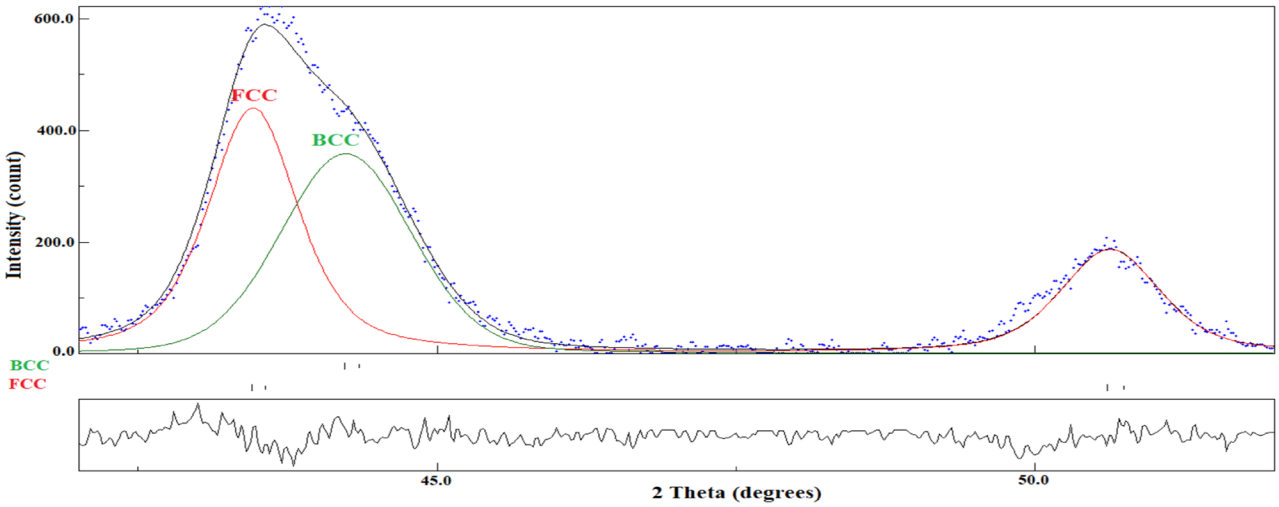

(b)

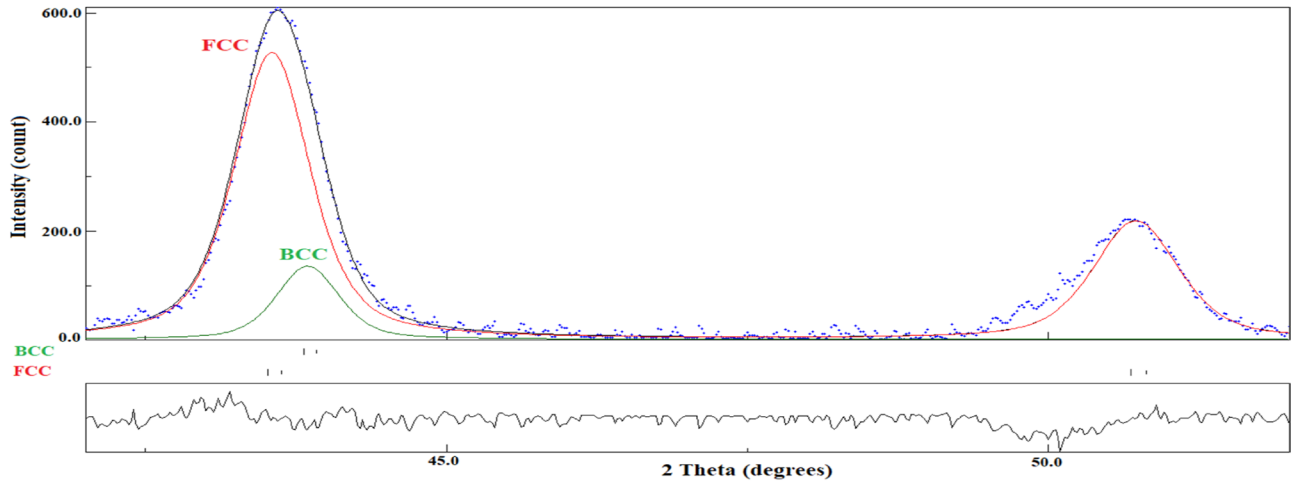

(c)

Fig. 4 Detailed scans for FCC and BCC phases; **a** HEA [39], **b** HEA + 5 wt% YSZnano, and **c** HEA + 10 wt% YSZnano samples

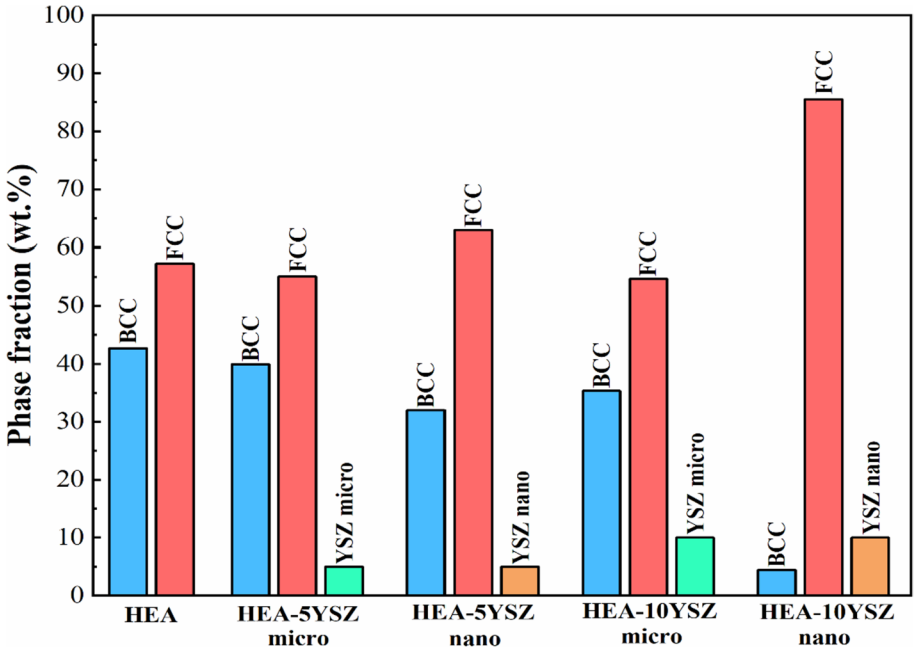

Fig. 5 Phase fraction of HEA-YSZmicro and HEA-YSZnano samples obtained from Rietveld refinement analysis

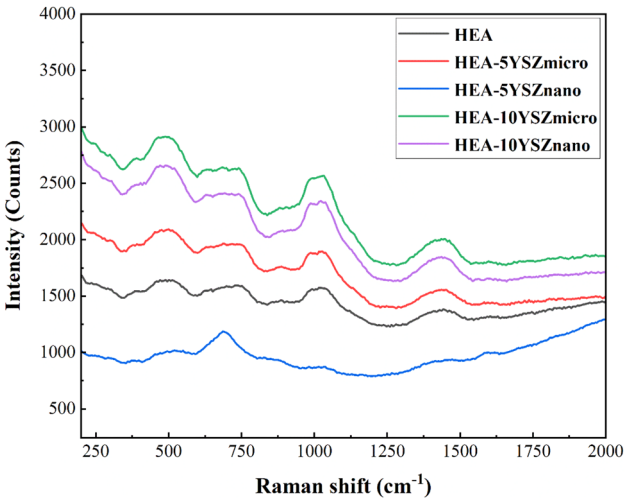

Fig. 6 Raman spectra of samples

The pin-on-disc wear machine (Abrasion Tester) available at Iran University of Science and Technology was utilized to evaluate the wear characteristics of the samples. The tests were conducted under ambient conditions, specifically at room temperature with a humidity level of 30%. The sliding was performed without the application of any lubrication. The counter pin used was a tungsten carbide ball with a diameter of 5 mm. The test parameters were set as follows: a fixed load of 30 N and a sliding speed of 0.07 m/s. The sliding distance for all the samples was standardized at 200 m. Each sample underwent three repetitions of the pin-on-disc test, and the average data for the friction coefficient and wear rate were recorded. It is important to note that the wear rate for each sample was calculated using the formula $k = V / (S \cdot F)$, where V shows the volume of mass loss, S represents the sliding distance, and F denotes the constant load.

3 Results and Discussion

3.1 Microstructure

The equiatomic HEA powder (after mechanical alloying) exhibits a BCC phase (Fig. 3a) due to the prevalence of BCC state in most of its constituent elements such as Fe, Cr, Co, and Al, whether occurring naturally (as in the case of Fe and Cr) or induced artificially (as high stresses during ball milling can lead to the manifestation of BCC structure in Co and Al elements). Following the heating process (SPS process), the unreinforced HEA sample undergoes a significant increase in the FCC phase (Fig. 3b), as the BCC to FCC transformation of this alloy takes place at approximately 650 °C [51, 52]. The XRD patterns of the HEAC samples, as shown in Fig. 3c-f, reveal some important features of the microstructure. Firstly, three phases (FCC, BCC, and oxide) are presented in the AlCoCrFeNi-YSZ composites at the same time. Secondly, the BCC peaks at 64.7° and 82.2° are absent in the last sample (HEA-10YSZ nano). Thirdly, the YSZ peak at 59° is absent in the nano-sized samples. In addition, the intensity of BCC peak at 44° decreases as the

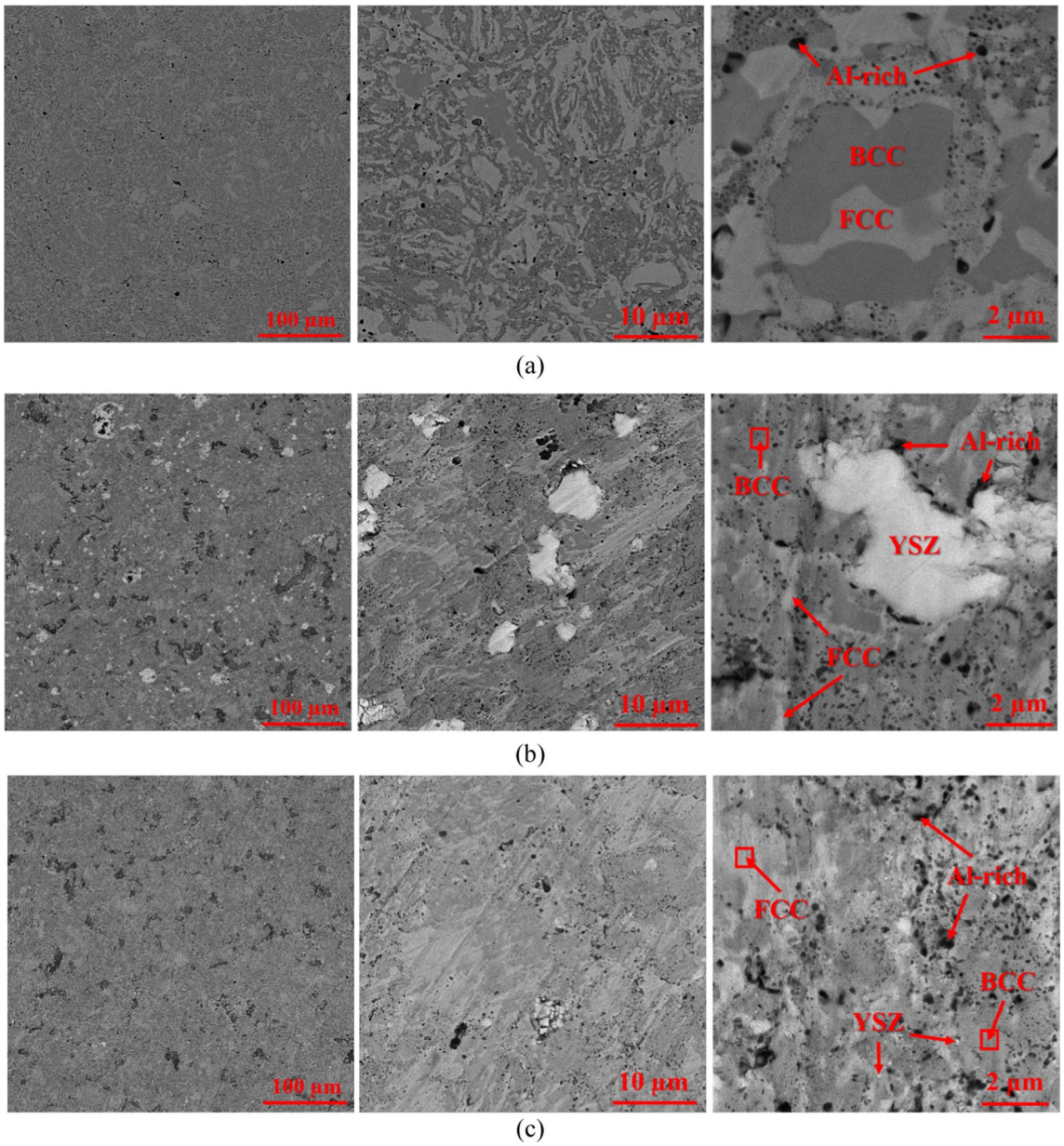

Fig. 7 SEM and FESEM images of **a** AlCoCrFeNi, **b** HEA-5 wt% YSZmicro, **c** HEA-5 wt% YSZnano, **d** HEA-10 wt% YSZmicro, and **e** HEA-10 wt% YSZnano

YSZ content increases and the YSZ size decreases. Since the BCC and FCC peaks overlap in the samples, the high-resolution XRD patterns in the range of 42° to 52° have been represented in Fig. 4. Furthermore, by performing Rietveld refinement analysis, the phase percentages for each sample are calculated and shown in Fig. 5. The results indicate that the BCC to FCC phase fraction is high in micro-sized ODS-HEACs (HEA-5YSZmicro and HEA-10YSZmicro), whereas this ratio is low in nano-sized ODS-HEACs, particularly in HEA-10YSZnano. Further, at the same oxide particle size, this ratio diminishes with an increase in YSZ content. Figure 6 demonstrates the clear presence of oxide bonds in the HEAC samples. While metallic samples typically do not exhibit Raman peaks [12, 25], the first sample (HEA) displays a few minor peaks associated with the minor content of oxides (AlO_x, FeO_x, and CrO_x phases) present in the sample. Upon the addition of YSZ particles in HEACs, there is an observed increase in the number of peaks and

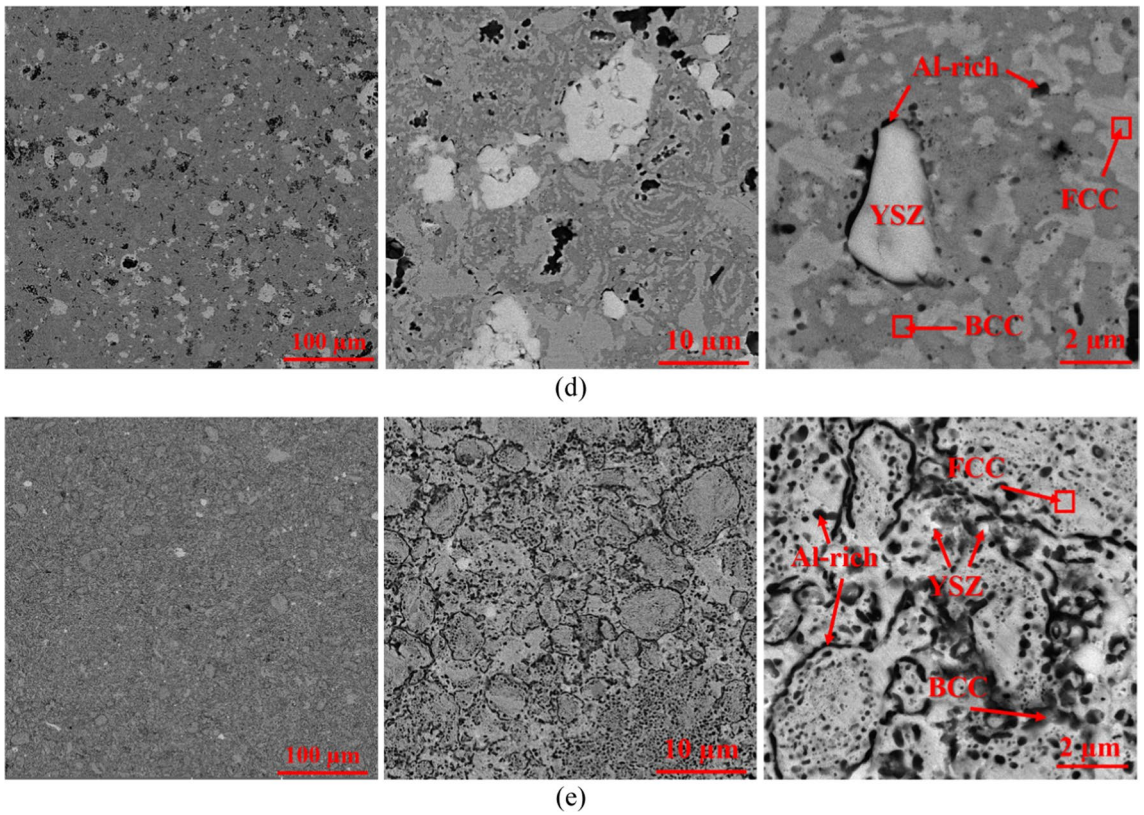

Fig. 7 (continued)

Table 1 EDS analysis results deduced from HEA-YSZ in different phases (in wt%)

Sample	Phase	Al	Co	Cr	Fe	Ni
HEA	FCC	5.71	24.88	22.24	28.04	19.13
	BCC	29.45	18.97	14.44	17.42	19.71
HEA-5YSZmicro	FCC	9.22	19.86	26.55	25.23	19.14
	BCC	18.36	17.96	10.35	16.89	32.10
HEA-5YSZnano	FCC	3.74	22.21	25.50	28.74	19.81
	BCC	19.90	19.59	6.76	13.65	40.10
HEA-10YSZmicro	FCC	4.32	26.21	23.45	29.40	16.63
	BCC	17.03	23.81	9.85	17.29	32.02
HEA-10YSZnano	FCC	6.34	24.92	21.64	23.43	23.67
	BCC	11.16	23.30	20.29	21.86	23.39

the height/intensity of the peaks. The broad peaks detected at 494 cm^{-1}, 510 cm^{-1}, 630 cm^{-1}, 671 cm^{-1}, 1010 cm^{-1}, 1398 cm^{-1}, and 1590 cm^{-1} are attributed to YSZ, Al_2O_3, YSZ, Cr_2O_3, Fe_2O_3, Fe_2O_3 and Cr_2O_3, respectively. This phenomenon is anticipated as it suggests an interaction of oxide bonds at different frequencies. Our analysis of peak locations closely aligns with that of other references [25, 53–57], exhibiting a high degree of concordance.

To understand the observed phase evolution in the prepared samples, SEM micrographs at different magnifications are presented in Fig. 7(a-e). In this figure, FCC, BCC, Al-rich, and reinforcement/YSZ phases are illustrated with arrows. It can be inferred that the grain size is larger in micro-sized ODS-HEACs. However, it is evident that YSZ particles are well dispersed in the micro-sized samples, while the dispersion of YSZ is not as effective in the nano-sized samples. Additionally, the elemental contribution of BCC and FCC phases is presented in Table 1. Based on the EDS elemental percentages, it is important to highlight that the composition of the BCC phase is rich in Ni and Al, while the FCC phase contrasts with a richness in Fe and Cr. The distribution of cobalt element is almost similar in both

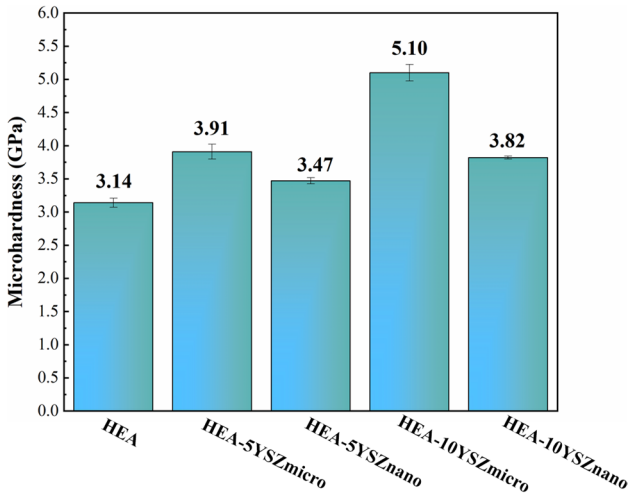

Fig. 8 Micro-hardness results

of FCC and BCC phases. Furthermore, the FCC phase fraction increases with the higher content of YSZ particles and reinforcement particle size reduction, which aligns well with the XRD-Rietveld analysis results. Among Al-Co-Cr-Fe–Ni elements, aluminum has the highest diffusion coefficient at the sintering temperature. Therefore, in the matrix-reinforcement interfaces, this element diffused out from Ni–Al-rich BCC phase toward interfacial regions. This leads to the evolution of the Al-rich zone in the microstructure and the reduction of BCC phase fraction in the composite samples. It should be noted that in the samples reinforced with nanometric YSZ particles which contain higher interfaces, the formation of the Al-rich phase is more pronounced. Therefore, the black regions at the interfaces consist of an Al-rich phase. However, due to the SPS process, other dispersed black areas (with low content) can be attributed to the presence of pores.

3.2 Mechanical Properties

Figure 8 illustrates the hardness data of AlCoCrFeNi-YSZ composites obtained from the Vickers hardness test. Several observations can be drawn directly from these data. Firstly, it is evident that oxide particles contribute to an increase in hardness. This finding holds true when comparing the hardness of HEA-10YSZmicro with the hardness of HEAs examined in other studies [4, 24]. Secondly, for the same YSZ size, a higher content of reinforcement leads to greater hardness. This finding aligns with the Vegard law, which posits that an increased presence of ceramic particles (due to their higher hardness and elastic modulus compared to metals) raises the average hardness of MMCs. Importantly, this result is consistent with prior studies [34, 41]. Thirdly, when holding the YSZ content constant, samples with micro-sized oxide particles exhibit higher hardness. This finding is complex and warrants further explanation, as multiple mechanisms come into play that can influence the mechanical properties. On one hand, the Hall–Petch mechanism and the smaller grain size of the nano-sized samples suggest higher hardness for HEA-5YSZnano/HEA-10YSZnano compared to HEA-5YSZmicro/HEA-10YSZmicro. However, on the other hand, factors such as solid solution, grain boundary, and Orowan strengthening mechanisms contradict the former mechanism. One contributing factor is the higher BCC phase fraction in micro-sized YSZ samples (as this phase has higher strength than FCC phases [24, 40]), leading to significant solid solution strengthening in these samples. Additionally, in MMCs with high metallic percentages, inter-type (micro-sized) strengthening prevails over intra-type (nano-sized) strengthening [58], resulting in higher fracture strength of micro-sized samples. This underscores the dominance of grain boundary strengthening in this scenario. Furthermore, due to the common occurrence of agglomeration of nanoparticles, YSZ dispersion is not perfect in nano-sized samples, limiting the dominance of the Orowan strengthening mechanism in these samples, while it can occur effectively in micro-sized samples.

Figure 9 displays the SEM images depicting the worn surfaces of the AlCoCrFeNi-YSZ composites. The wear width and specific wear rate data derived from these images are presented in Fig. 10. A comparison of the wear widths/rates of the HEAC samples and the HEA sample [26] indicates the advantageous influence of oxide dispersion strengthening on the wear characteristics. This result is consistent with findings from previous studies [40, 50]. Furthermore, it is noteworthy that the wear characteristics of the samples with micro-sized YSZ are superior to those with nano-sized YSZ. Additionally, a higher content of oxide particles can result in increased wear resistance. This can be attributed to the elevated hardness level, which can lead to increased wear resistance [21, 47, 48]. For a detailed examination of wear patterns, higher resolution SEM images of each ODS-HEAC have presented in Fig. 11. These images reveal the involvement of multiple wear mechanisms such as oxidation (as indicated by the high oxygen content in Fig. 12 or high-intensity oxide bonds in Fig. 13), abrasion (with ploughing grooves) and adhesion-delamination (with debris and cracks underneath). To explain the latter more, according to the high pin load-low sliding speed, it is possible for localized and minor welding and adhesion to occur as a result of friction welding. This adhesive mechanism is supported by the EDS results depicted in Fig. 12, which show tungsten entering from the pin to the worn surface. The wear mechanisms mentioned commonly occur in high entropy

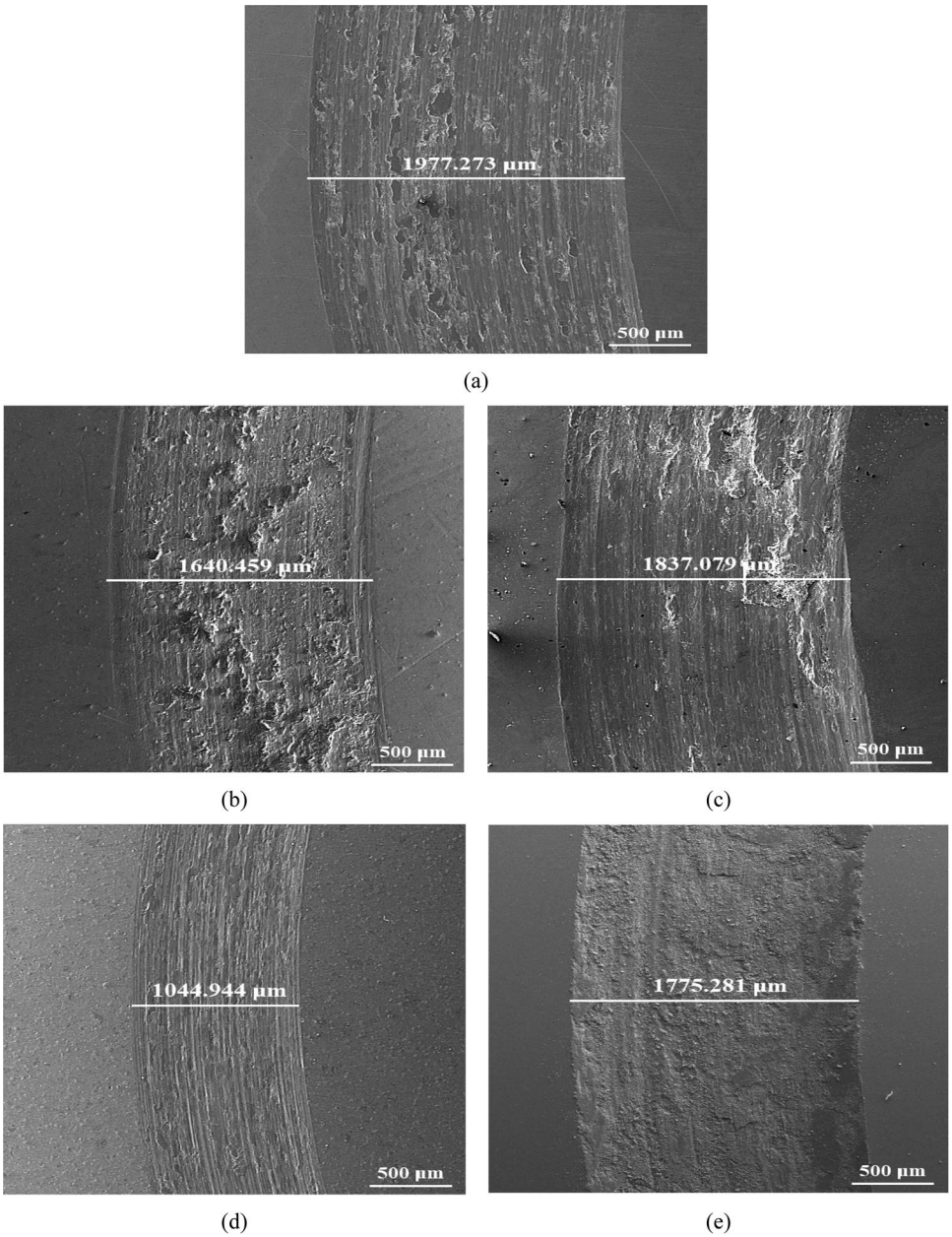

Fig. 9 SEM images related to wear tracks of the composite samples; **a** HEA, **b** HEA-5 wt% YSZmicro, **c** HEA-5 wt% YSZnano, **d** HEA-10 wt% YSZmicro, and **e** HEA-10 wt% YSZnano

alloys [25]. In Fig. 13, the Raman broad peaks observed at 502 cm^{-1}, 530 cm^{-1}, 626 cm^{-1}, 668 cm^{-1}, 1391 cm^{-1}, and 1590 cm^{-1} correspond to Al_2O_3, Cr_2O_3, YSZ, Al_2O_3, Fe_2O_3, and Cr_2O_3, respectively. These results are accordant with findings from other studies [25, 53–57]. These oxide peaks (excluding the one corresponding to YSZ) indicate a higher level of oxidation reaction at the surface of the HEAC samples during sliding. It is evident that samples with higher wear rates (HEA, HEA-5YSZnano, and HEA-10YSZnano) exhibit significant amounts of delamination and oxidation mechanisms. In the case of HEA-5YSZnano, long ploughing grooves demonstrate substantial abrasion wear phenomena. These results demonstrate that, similar to findings in other reference [30], the addition of ceramic particles to HEAs not only enhances hardness, but also reduces wear rates, which are highly desirable outcomes.

It should be noted that certain types of defects, such as pores and impurities (e.g., oxide phases), can form during the mechanical alloying and subsequent SPS processing of metal matrix composites. However, demonstrating the impact of these defects on the mechanical properties of HEACs poses a challenge and necessitates more comprehensive investigations, including techniques like atom probe tomography, 3D-EBSD, and TEM analyses. Nevertheless, in the case of HEA + YSZ composites, the influence of these defects on mechanical properties can be considered negligible for two primary reasons. First, the analysis of XRD, EDS, Raman, and SEM results suggests that the proportion of pores and impurities is not significant. Second, the similarity in pore fraction and impurity percentages across all samples indicates that these defects have not markedly influenced the mechanical properties.

Additionally, the variation in friction coefficient for each sample is presented in Fig. 14. Due to considerable fluctuations in the CoF results, and to make the curves comparable, the trend line has been fitted for each graph. In Fig. 14b, the initial wear stage (running-in period) of each sample has been excluded. It is evident that HEA-10YSZmicro exhibits the lowest coefficient of friction (CoF). Furthermore, unlike the other samples which display significant CoF fluctuations, HEA-10YSZmicro demonstrates a steady-state trend, potentially leading to lower friction and dissipation energy. According to the formula presented in the reference [59], a lower CoF may result in a decrease in temperature rise and dissipation energy. As a consequence, this can potentially mitigate issues such as deformation, detachment, and cracking caused by thermal variations. Consequently, as shown in Fig. 10, HEA-10YSZmicro exhibits the minimum wear width and rate. The desired wear characteristics of HEA-10YSZmicro become particularly significant when considering the high normal load (30 N)/contact stresses (more than 2.4 GPa), especially in comparison to experiments conducted

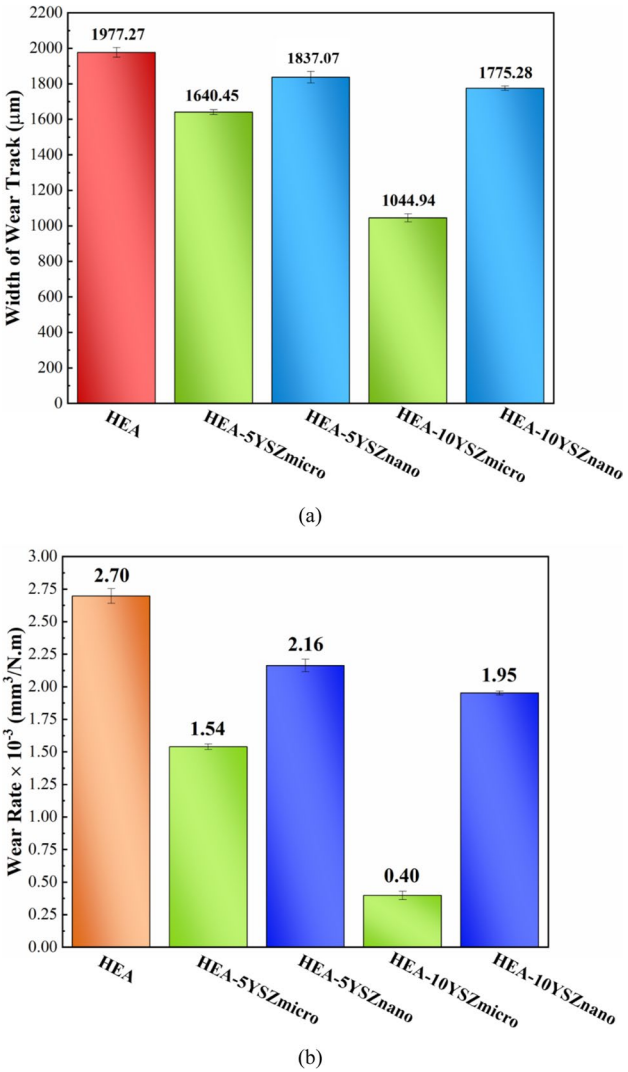

Fig. 10 **a** average wear width and **b** wear rate of samples

in other studies [4, 6] using lower loads/contact stresses (typically less than 20 N). The stresses are computed using the Hertzian contact pressure equation (Eqs. 1 and 2) [60], in which F represents the normal load (N) and R denotes the radius of the pin (mm). Additionally, υ_i and E_i refer to the Poisson's ratio and Young's modulus of the sample or counterpart (the Poisson's ratio for the samples is regarded as 0.25, while for tungsten carbide it is 0.3 and the Young's modulus of tungsten carbide is 560 GPa). Therefore, this material emerges as a promising candidate for use in mechanical components subjected to erosion and wear.

$$\text{Contact stress} = \left(6F/\pi^3 R^3 E *^2\right)^{1/3} \quad (1)$$

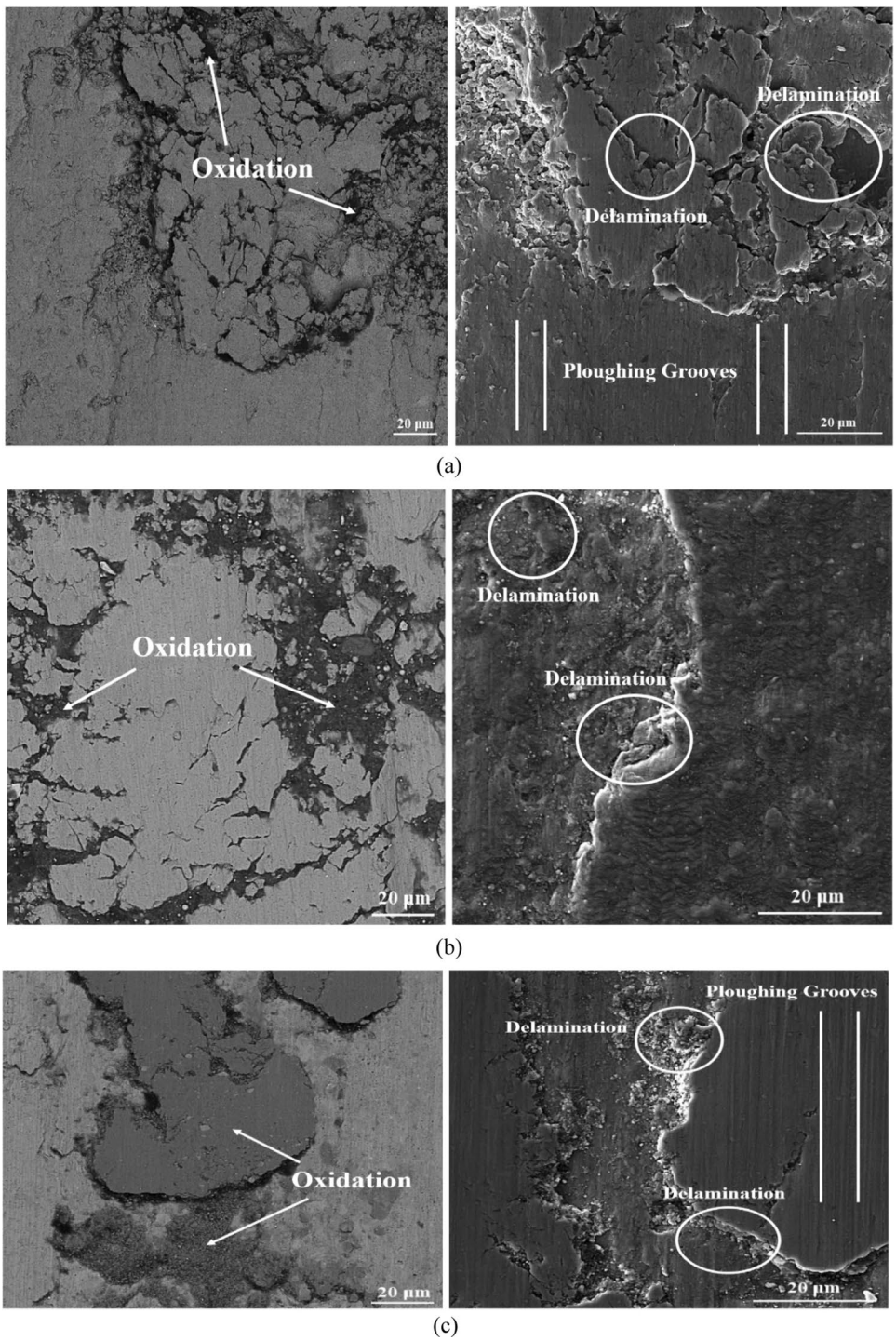

Fig. 11 SEM micrographs of the worn surfaces of samples; **a** HEA, **b** HEA-5 wt% YSZmicro, **c** HEA-5 wt% YSZnano, **d** HEA-10 wt% YSZmicro, and **e** HEA-10 wt% YSZnano

Fig. 11 (continued)

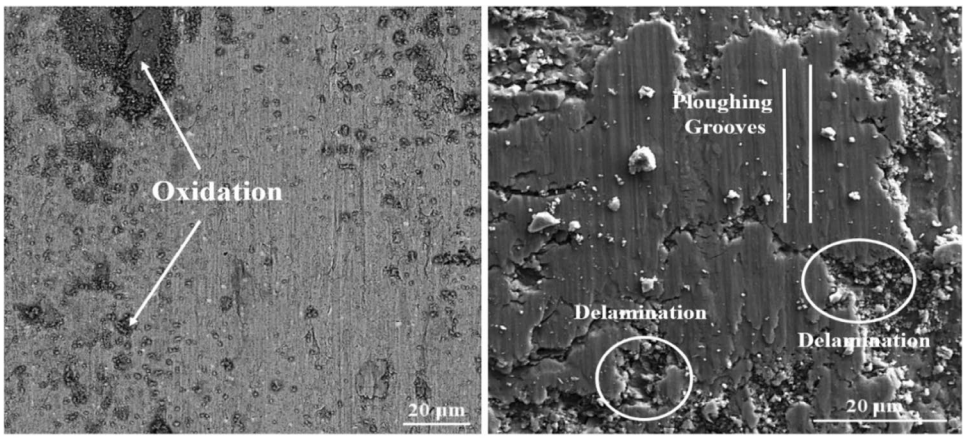

(d)

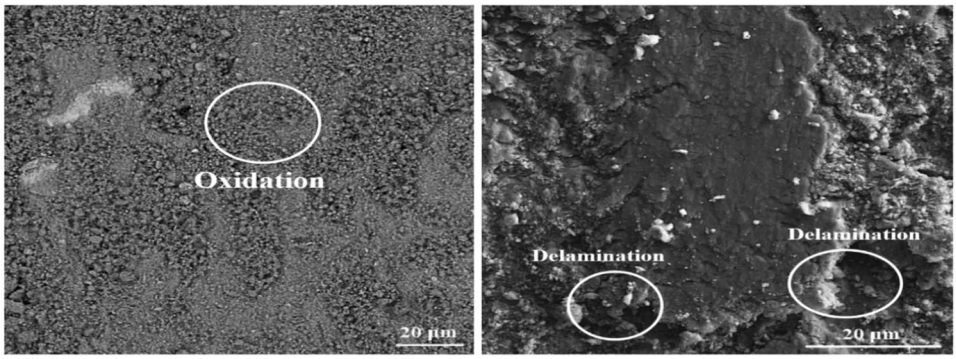

(e)

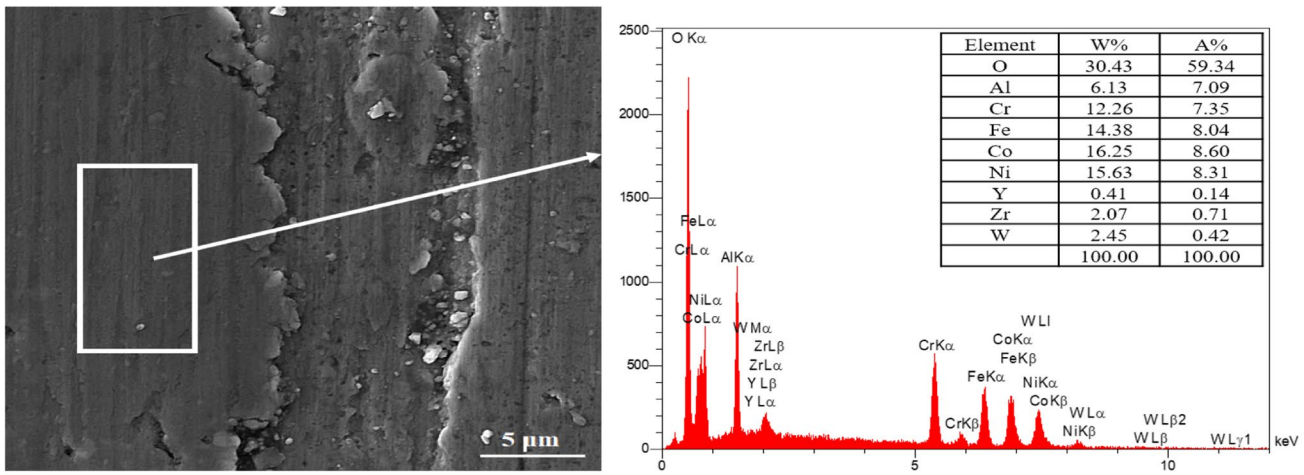

(a)

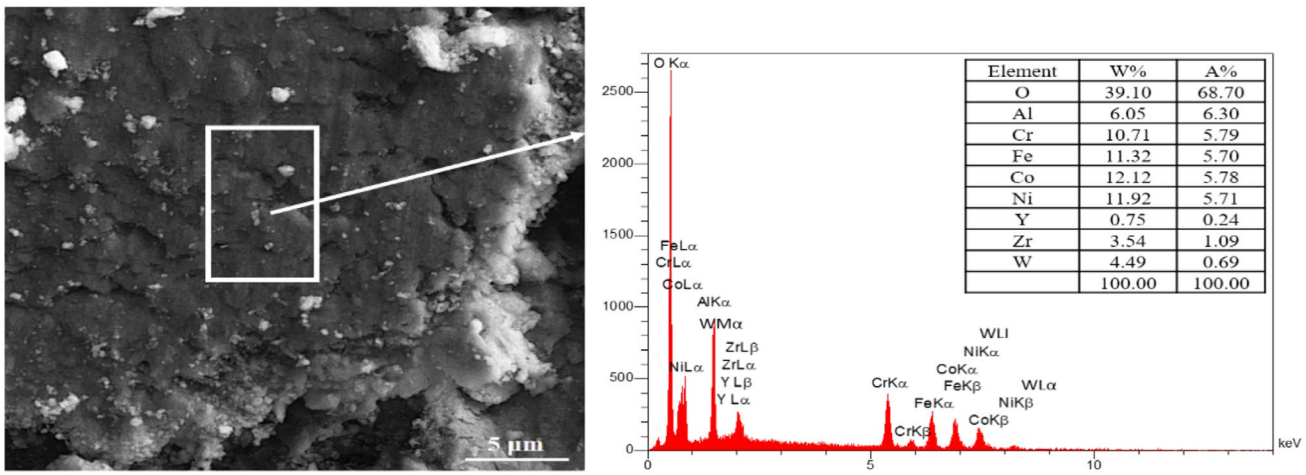

(b)

Fig. 12 EDS analysis of the worn surfaces of samples; **a** HEA-5 wt% YSZnano and **b** HEA-10 wt% YSZnano

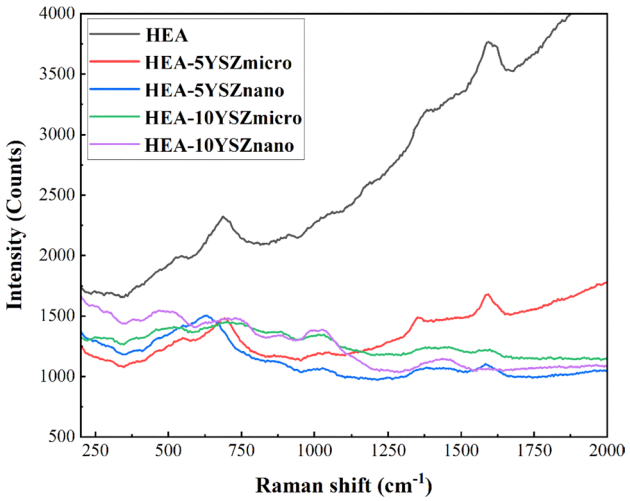

Fig. 13 Raman spectra of worn samples

$$\frac{1}{E^*} = \frac{1-v_1^2}{E_1} + \frac{1-v_2^2}{E_2} \quad (2)$$

4 Conclusions

The microstructure and mechanical properties of AlCoCrFeNi high entropy alloys with varying YSZ size and content have been investigated through a series of tests. The composite phase structure (FCC + BCC + YSZ), as well as hardness and wear behaviors, exhibit significant variation when the size and content of oxide particles are altered. Consequently, it can be inferred that:

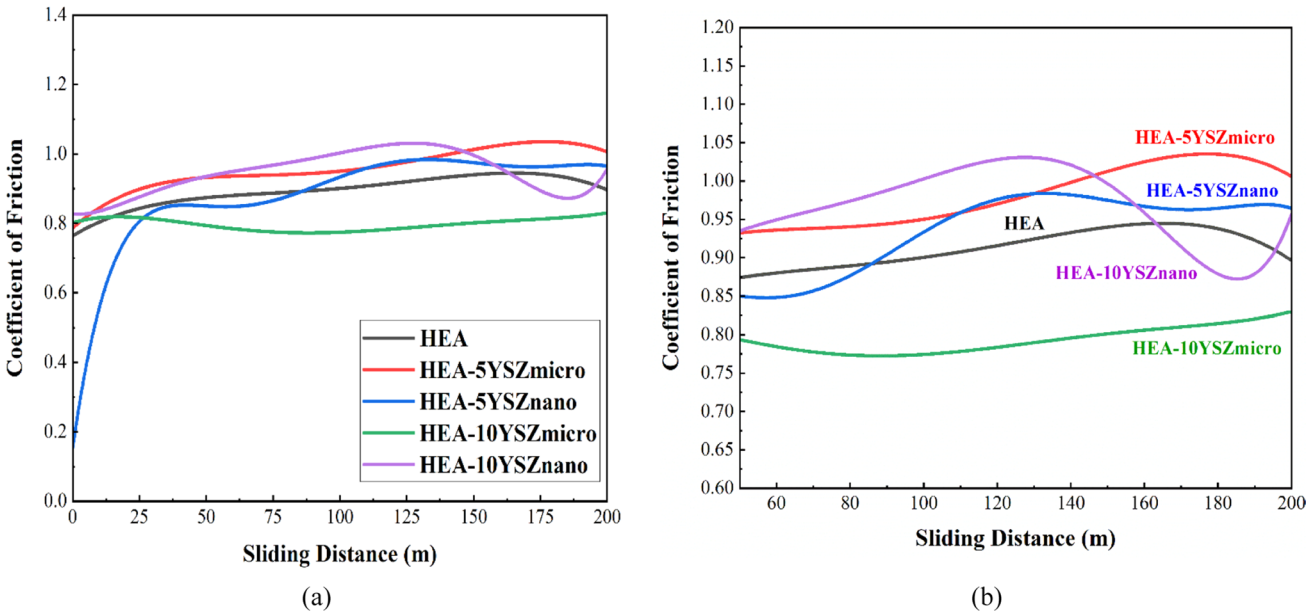

Fig. 14 Fitted curves of CoF for each sample; **a** total variations **b** without running-in period

1. Based on the XRD and SEM–EDS results, the level of BCC to FCC ratio is found to be strongly correlated with the YSZ content in ODS-HEAC samples. The ratio of BCC to FCC is higher in micro-sized YSZ samples compared to nano-sized YSZ samples, with the lowest ratio observed in the HEA-10YSZnano sample.
2. According to the Raman results, it is clear that oxidation can happen during the sintering of powders. Moreover, under sliding conditions, oxide content at the surface can be increased especially in the case of metallic sample (HEA).
3. At the same oxide particle size, when the YSZ content increases hardness increases and wear rate decreases which is desirable behavior.
4. At the same oxide particle content, micro-sized YSZ samples show higher hardness and lower wear width. This behavior can be attributed to multiple mechanisms.
5. Under high load and contact stresses, HEA-10YSZmicro shows steady-state wear and a low friction coefficient (the average is 0.8). Other samples show fluctuations and higher friction coefficients (their average is more than 0.92).

Declarations

Conflict of Interest None.

References

1. A.O. Mekhrabov, M.V. Akdeniz, Effect of ternary alloying elements addition on atomic ordering characteristics of Fe–Al intermetallics. Acta Mater. **47**(7), 2067–2075 (1999)
2. J.-W. Yeh, S.-K. Chen, S.-J. Lin, J.-Y. Gan, T.-S. Chin, T.-T. Shun, C.-H. Tsau, S.-Y. Chang, Nanostructured high-entropy alloys with multiple principal elements: novel alloy design concepts and outcomes. Adv. Eng. Mater. **6**(5), 299–303 (2004)
3. Z. Li, K.G. Pradeep, Y. Deng, D. Raabe, C.C. Tasan, Metastable high-entropy dual-phase alloys overcome the strength–ductility trade-off. Nature **534**(7606), 227–230 (2016)
4. J. Miao, H. Liang, A. Zhang, J. He, J. Meng, Y. Lu, Tribological behavior of an $AlCoCrFeNi_{2.1}$ eutectic high entropy alloy sliding against different counterfaces. Tribol. Int. **153**, 106599 (2021)
5. Y.A. Alshataif, S. Sivasankaran, F.A. Al-Mufadi, A.S. Alaboodi, H.R. Ammar, Manufacturing methods, microstructural and mechanical properties evolutions of high-entropy alloys: a review. Met. Mater. Int. **26**(8), 1099–1133 (2020)
6. X. Li, Y. Wang, F. Wang, A. Liang, Subsonic-flame-sprayed CoCrFeNi, AlCoCrFeNi and MnCoCrFeNi-based high-entropy alloy coatings and their tribological behaviors. J. Therm. Spray Technol. **32**(1), 96–110 (2023)
7. Y. Wang, R. Wang, J. Lin, L. Wang, Z. Chen, Mechanical and high-temperature wear resistance properties of WC-reinforced $AlCoCrFeNiTi_{0.5}$ high entropy alloy matrix composite. Ceram. Int. **50**(1), 2162–2176 (2024)
8. K.R. Rao, S.K. Dewangan, A.H. Seikh, S.K. Sinha, B. Ahn, Microstructure and mechanical characteristics of AlCoCrFeNi-based ODS high-entropy alloys consolidated by vacuum hot pressing. Met. Mater. Int. **30**(3), 726–734 (2024)
9. Ł Rogal, Z. Szklarz, P. Bobrowski, D. Kalita, G. Garzeł, A. Tarasek, M. Kot, M. Szlezynger, Microstructure and mechanical properties of Al–Co–Cr–Fe–Ni base high entropy alloys obtained using powder metallurgy. Met. Mater. Int. **25**(4), 930–945 (2019)

10. J. Feng, Y. Tang, J. Liu, P. Zhang, C. Liu, L. Wang, Bio-high entropy alloys: progress, challenges, and opportunities. Front. Bioeng. Biotechnol. **10**, 977282 (2022)
11. M.C. Gao, J.-W. Yeh, P.K. Liaw, Y. Zhang (eds), High-Entropy Alloys: Fundamentals and Applications (Springer, Cham,2016).
12. P. Zhou, P.K. Wong, P. Niu, M. Chen, C.T. Kwok, Y. Tang, R. Li, S. Wang, H. Pan, Anodized AlCoCrFeNi high-entropy alloy for alkaline water electrolysis with ultra-high performance. Sci. China Mater. **66**(3), 1033–1041 (2023)
13. S.K. Dewangan, A. Mangish, S. Kumar, A. Sharma, B. Ahn, V. Kumar, A review on high-temperature applicability: a milestone for high entropy alloys. Eng. Sci. Technol. Int. J. **35**, 101211 (2022)
14. D.B. Miracle, O.N. Senkov, A critical review of high entropy alloys and related concepts. Acta Mater. **122**, 448–511 (2017)
15. Y.F. Ye, Q. Wang, J. Lu, C.T. Liu, Y. Yang, High-entropy alloy: challenges and prospects. Mater. Today **19**(6), 349–362 (2016)
16. T. Fujieda, H. Shiratori, K. Kuwabara, M. Hirota, T. Kato, K. Yamanaka, Y. Koizumi, A. Chiba, S. Watanabe, CoCrFeNiTi-based high-entropy alloy with superior tensile strength and corrosion resistance achieved by a combination of additive manufacturing using selective electron beam melting and solution treatment. Mater. Lett. **189**, 148–151 (2017)
17. J. Fan, W. Zhang, Atomic scale diffusion study in quaternary and quinary alloys of Co–Cr–Fe–Mn–Ni system. Met. Mater. Int.30(2), 457–468 (2024)
18. H. Zheng, R. Chen, G. Qin, X. Li, Y. Su, H. Ding, J. Guo, H. Fu, Microstructure evolution, Cu segregation and tensile properties of CoCrFeNiCu high entropy alloy during directional solidification. J. Mater. Sci. Technol. **38**, 19–27 (2020)
19. H. Yang, J. Li, T. Guo, W.Y. Wang, H. Kou, J. Wang, Fully recrystallized $Al_{0.5}$CoCrFeNi high-entropy alloy strengthened by nanoscale precipitates. Met. Mater. Int. **25**(5), 1145–1150 (2019)
20. A. Shafiei, Design of eutectic high entropy alloys in Al–Co–Cr–Fe–Ni system. Met. Mater. Int. **27**(1), 127–138 (2021)
21. J.-M. Wu, S.-J. Lin, J.-W. Yeh, S.-K. Chen, Y.-S. Huang, H.-C. Chen, Adhesive wear behavior of Al_xCoCrCuFeNi high-entropy alloys as a function of aluminum content. Wear **261**(5), 513–519 (2006)
22. C.T. Wang, Y. He, Z. Guo, X. Huang, Y. Chen, H. Zhang, Y. He, Strain rate effects on the mechanical properties of an AlCoCrFeNi high-entropy alloy. Met. Mater. Int. **27**(7), 2310–2318 (2021)
23. L. Guo, D. Xiao, W. Wu, S. Ni, M. Song, Effect of Fe on microstructure, phase evolution and mechanical properties of $(AlCoCrFeNi)_{100-x}Fe_x$ high entropy alloys processed by spark plasma sintering. Intermetallics **103**, 1–11 (2018)
24. T.-T. Shun, W.-J. Hung, Effects of Cr content on microstructure and mechanical properties of $AlCoCr_xFeNi$ high-entropy alloy. Adv. Mater. Sci. Eng. **2018**, 5826467 (2018)
25. Y. Wang, X. Li, A. Liang, Wear behavior and microstructural transformation of single fcc phase AlCoCrFeNi high-entropy alloy at elevated temperatures. Int. J. Mater. Res. **113**(8), 730–743 (2022)
26. A. Faraji, M. Farvizi, T. Ebadzadeh, H.S. Kim, Microstructure, wear performance, and mechanical properties of spark plasma-sintered AlCoCrFeNi high-entropy alloy after heat treatment. Intermetallics **149**, 107656 (2022)
27. S. Praveen, B.S. Murty, R.S. Kottada, Phase evolution and densification behavior of nanocrystalline multicomponent high entropy alloys during spark plasma sintering. JOM **65**(12), 1797–1804 (2013)
28. I. Basu, V. Ocelík, J.T. De Hosson, BCC-FCC interfacial effects on plasticity and strengthening mechanisms in high entropy alloys. Acta Mater. **157**, 83–95 (2018)
29. M. Farvizi, M. Bahamirian, A. Faraji, H.S. Kim, Role of particle size of Al_2O_3 reinforcement on the wear performance of NiTi-based composites. Met. Mater. Int. **28**, 101726 (2023)
30. R. Zhou, G. Chen, B. Liu, J. Wang, L. Han, Y. Liu, Microstructures and wear behaviour of $(FeCoCrNi)_{1-x}(WC)_x$ high entropy alloy composites. Int. J. Refract Metal Hard Mater. **75**, 56–62 (2018)
31. D. Yim, P. Sathiyamoorthi, S.-J. Hong, H.S. Kim, Fabrication and mechanical properties of TiC reinforced CoCrFeMnNi high-entropy alloy composite by water atomization and spark plasma sintering. J. Alloy. Compd. **781**, 389–396 (2019)
32. B. Li, L. Zhang, Y. Xu, Z. Liu, B. Qian, F. Xuan, Selective laser melting of CoCrFeNiMn high entropy alloy powder modified with nano-TiN particles for additive manufacturing and strength enhancement: process, particle behavior and effects. Powder Technol. **360**, 509–521 (2020)
33. L. Zong, L. Xu, C. Luo, Z. Jiao, X. Li, W. Sun, S. Wei, Mechanical properties and strengthening mechanism of the nano-sized m-ZrO_2 ceramic particle reinforced NbMoTaW refractory high-entropy alloy. Int. J. Refract Metal Hard Mater. **113**, 106201 (2023)
34. S. Yang, X. Yan, K. Yang, Z. Fu, Effect of the addition of nano-Al2O3 on the microstructure and mechanical properties of twinned $Al_{0.4}FeCrCoNi_{1.2}Ti_{0.3}$ alloys. Vacuum **131**, 69–72 (2016)
35. B. Gwalani, R.M. Pohan, O.A. Waseem, T. Alam, S.H. Hong, H.J. Ryu, R. Banerjee, Strengthening of $Al_{0.3}$CoCrFeMnNi-based ODS high entropy alloys with incremental changes in the concentration of Y_2O_3. Scr. Mater. **162**, 477–481 (2019)
36. M. Farvizi, T. Ebadzadeh, M.R. Vaezi, E.Y. Yoon, Y.J. Kim, H.S. Kim, A. Simchi, Microstructural characterization of HIP consolidated NiTi–nano Al_2O_3 composites. J. Alloy. Compd. **606**, 21–26 (2014)
37. U. Mücke, Ceramic microstructures. Property control by processing. von W. E. Lee und W. M. Rainforth, 590 Seiten,Zahlreiche Abbildungen, Chapman & Hall, London, Glasgow, Weinheim. New York, Tokio, Melbourne, Madras, 1994, £ 89.00,ISBN 0-412-43140-8. Mater. Corros. 47(6), 346–347 (1996).
38. M. Woydt, A. Skopp, I. Dörfel, K. Witke, Wear engineering oxides/anti-wear oxides. Wear **218**(1), 84–95 (1998)
39. M. Ghanbariha, M. Farvizi, T. Ebadzadeh, Microstructural development in nanostructured AlCoCrFeNi–ZrO_2 high-entropy alloy composite prepared with mechanical alloying and spark plasma sintering methods. Mater. Res. Express **6**(12), 1265b5 (2019)
40. M. Ghanbariha, M. Farvizi, T. Ebadzadeh, A. Alizadeh Samiyan, Effect of ZrO_2 particles on the nanomechanical properties and wear behavior of AlCoCrFeNi–ZrO_2 high entropy alloy composites. Wear **484**, 204032 (2021)
41. T. Liao, Y.-K. Cao, W.-M. Guo, Q.-H. Fang, J. Li, B. Liu, Microstructure and mechanical property of NbTaTiV refractory high-entropy alloy with different Y_2O_3 contents. Rare Met. **41**(10), 3504–3514 (2022)
42. A. Sanaty-Zadeh, Comparison between current models for the strength of particulate-reinforced metal matrix nanocomposites with emphasis on consideration of Hall–Petch effect. Mater. Sci. Eng. A **531**, 112–118 (2012)
43. Z. Zhang, Y.H. Xie, X.Y. Huo, S.L.I. Chan, J.M. Liang, Y.F. Luo, D.K.Q. Mu, J. Ju, J. Sun, J. Wang, Microstructure and mechanical properties of ultrafine grained CoCrFeNi and $CoCrFeNiAl_{0.3}$ high entropy alloys reinforced with $Cr2O3/Al2_{O.3}$ nanoparticles. Mater. Sci. Eng. A **816**, 141313 (2021)
44. F.S. Kaplan, I.G. Shulik, L.S. Alekseenko, G.P. Orekhova, Properties of slips of zirconia stabilized by oxides of rare earth metals. Refractories **36**(3), 82–85 (1995)
45. O.A. Graeve, Zirconia, in *Ceramic and Glass Materials: Structure, Properties and Processing*, ed. by J.F. Shackelford, R.H.Doremus (Springer, New York, 2008), pp. 169–197

46. G.P. Cousland, X.Y. Cui, A.E. Smith, A.P.J. Stampfl, C.M. Stampfl, Mechanical properties of zirconia, doped and undoped yttria-stabilized cubic zirconia from first-principles. J. Phys. Chem. Solids **122**, 51–71 (2018)
47. S.A. Ataie, R. Keshtmand, M.R. Zamani-Meymian, Nanomechanical properties of Cr-Zr-Nb-N medium entropy alloy films produced by reactive sputtering. Int. J. Refract Metal Hard Mater. **110**, 106006 (2023)
48. S.A. Ataie, M. Soltanieh, R. Naghizadeh, A. Cavaleiro, M. Evaristo, F. Fernandes, F. Ferreira, Effect of substrate bias voltage on structural and tribological properties of W-Ti-C-N thin films produced by combinational HiPIMS and DCMS co-sputtering. Wear **520–521**, 204654 (2023)
49. R. Liu, D.Y. Li, Y.S. Xie, R. Llewellyn, H.M. Hawthorne, Indentation behavior of pseudoelastic TiNi alloy. Scripta Mater. **41**(7), 691–696 (1999)
50. K. Raja, P. Ganeshan, B.K. Singh, R.K. Upadhyay, P. Ramshankar, V. Mohanavel, Effect of mol% of Yttria in Zirconia matrix alongside a comparative study among YSZ, alumina & ZTA ceramics in terms of mechanical and functional properties. Sādhanā **48**(2), 72 (2023)
51. G. Fiquet, C. Narayana, C. Bellin, A. Shukla, I. Estève, A.L. Ruoff, G. Garbarino, M. Mezouar, Structural phase transitions in aluminium above 320GPa. C.R. Geosci. **351**(2), 243–252 (2019)
52. S.A. Makhlouf, E. Ivanov, K. Sumiyama, K. Suzuki, Structural and magnetic properties of nanocrystalline b.c.c. cobalt particles obtained by leaching of mechanically alloyed Co Al. J. Alloys Compd. **189**(1), 117–121 (1992)
53. S. Tailor, M. Singh, A.V. Doub, Synthesis and characterization of yttria-stabilized zirconia (YSZ) nano-clusters for thermal barrier coatings (TBCs) applications. J. Clust. Sci. **27**(4), 1097–1107 (2016)
54. B.P. Dhonge, T. Mathews, S. Rajagopalan, S. Dash, S. Dhara, A.K. Tyagi, Cubic fluorite yttria stabilized zirconia (YSZ) filmsynthesis by combustion chemical vapour deposition(C-CVD), in *Proceedings of the International Conference on Nanoscience,Engineering and Technology (ICONSET 2011)*, Chennai, 28-30 November 2011 (IEEE, New York, 2011), pp. 65–68
55. J. Yang, W.N. Martens, R.L. Frost, Transition of chromium oxyhydroxide nanomaterials to chromium oxide: a hot-stage Raman spectroscopic study. J. Raman Spectrosc. **42**(5), 1142–1146 (2011)
56. K. Song, Y. Lee, M.R. Jo, K.M. Nam, Y.-M. Kang, Comprehensive design of carbon-encapsulated Fe3O4 nanocrystals and their lithium storage properties. Nanotechnology **23**(50), 505401 (2012)
57. S. Benafia, D. Retraint, S. Yapi Brou, B. Panicaud, J.L. Grosseau Poussard, Influence of surface mechanical attrition treatment on the oxidation behaviour of 316L stainless steel. Corros. Sci. **136**, 188–200 (2018)
58. C. Laurent, A. Rousset, Metal-oxide ceramic matrix nanocomposites. Key Eng. Mater. **108–110**, 405–406 (1995)
59. M. Bai, L. Yang, J. Li, L. Luo, S. Sun, B. Inkson, Mechanical and tribological properties of Si and W doped diamond like carbon (DLC) under dry reciprocating sliding conditions. Wear **484–485**, 204046 (2021)
60. X. Liu, Y. Wang, L. Qin, Z. Guo, Z. Lu, X. Zhao, H. Dong, Q. Xiao, Friction and wear properties of a novel interface of ordered microporous Ni-based coating combined with MoS_2 under complex working conditions. Tribol. Int. **189**, 108970 (2023)